VOL. 4, NO. 6 J. PROPULSION NOV.-DEC. 1988

Numerical Study of the Interactions Between Droplets at Intermediate Reynolds Numbers

Jian-Shun Shuen*
NASA Lewis Research Center, Cleveland, Ohio

Effects of droplet interactions on drag, evaporation, and combustion of a planar droplet array oriented perpendicular to the approaching flow are studied numerically. The three-dimensional Navier-Stokes equations, with variable thermophysical properties, are solved using finite-difference techniques. Parameters investigated include the droplet spacing, droplet Reynolds number, approaching stream oxygen concentration, and fuel type. Results are obtained for a Reynolds number range of 5 to 100, droplet spacings from 2 to 24 diameters, oxygen concentrations of 0.1 and 0.2, and methanol and *n*-butanol fuels. The calculations show that gasification rates of interacting droplets decrease as droplet spacings decrease. The reduction in gasification rates is significant only at small spacings and low Reynolds numbers. The effects of adjacent droplets on drag are shown to be small for the present array orientation.

Nomenclature

B = heat-transfer number, $C_p(T_\infty - T_s)/h_{fg}$ for vaporizing droplet
C_D = total drag coefficient, $= \dfrac{\text{total drag}}{\pi d_p^2 \rho_\infty u_\infty^2/8}$
C_f = friction drag coefficient, $= \dfrac{\text{total friction force}}{\pi d_p^2 \rho_\infty u_\infty^2/8}$
C_p = pressure drag coefficient, $= \dfrac{\text{total pressure force}}{\pi d_p^2 \rho_\infty u_\infty^2/8}$
c_p = specific heat
$\mathscr{D}_i$ = mass diffusivity of species i in the gas mixture
d_p = droplet diameter
e = total internal energy per unit volume
f = mixture fraction, defined as the mass that originated from the droplets per unit mass of the gas mixture
H = heat-transfer coefficient, Eq. (19)
h = enthalpy
h_{fg} = heat of vaporization
h_f^0 = heat of formation
J = Jacobian of the coordinate transformation
k = thermal conductivity
M = molecular weight
N_S = number of species
Nu = Nusselt number, $= Hd_p/k$
p = pressure
Pr = Prandtl number, $= c_p\mu/k$
q = heat flux
r_p = droplet radius
Re = droplet Reynolds number, $= \rho_\infty q_\infty d_p/\mu_\infty$
Re_m = droplet Reynolds number, $= \rho_\infty q_\infty d_p/\mu_m$
$\tilde{R}$ = universal gas constant
S = nondimensional droplet spacing, normalized by d_p
T = temperature
t = time
U,V,W = contravariant velocity, Eq. (3)
u,v,w = Cartesian velocity components in x (axial), y, and z directions, respectively
X,Y = mole and mass fractions, respectively
x,y,z = Cartesian coordinates, Fig. 1
α = weighting factor, Eq. (18)
β = gasification rate correction factor, $\beta = \dfrac{\text{rate of gasification of a droplet in an array}}{\text{rate of gasification of an isolated droplet}}$
ζ,η,ξ = generalized curvilinear coordinates
θ = angle along the droplet surface measured from the front stagnation point
μ = viscosity
ν = stoichiometric coefficient (by mass) of oxygen
ρ = density
τ = stress tensor
Ω = oxygen concentration in the approaching stream

Subscripts

A = air property
F = fuel property
i = index of species
m = film condition
N_2 = nitrogen
O_2 = oxygen
prod = combustion product property
s = droplet surface condition
stoic = stoichiometric condition
UF = unburned fuel property
v = viscous flux term
x,y,z = derivatives in x, y, and z directions, respectively
∞ = approaching flow condition

Introduction

THE evaporation and combustion of liquid fuel sprays have received considerable attention. Much of the theoretical work has focused on the transport of single isolated droplets.[1-3] In dense sprays found in regions near the fuel nozzle, droplets may evaporate and burn quite differently than isolated droplets.[2-6] Various coupled physical processes occur in the dense-spray region, including atomization, droplet collision, coalescence, breakup, modification of turbulence properties by the droplets, and interphase transport processes, etc. In the present study, droplet interactions (defined as the modification of droplet transport rates due to the presence of adjacent droplets) are numerically investigated.

Presented as Paper 87-0137 at the AIAA 25th Aerospace Sciences Meeting, Reno, NV, Jan. 12-15, 1987; received April 27, 1987; revision received Sept. 15, 1987.

*Senior Research Engineer. Member AIAA.

Previous theoretical studies on droplet interactions have been limited largely to droplets in arrays or clouds in the absence of forced convection (hereinafter referred to as diffusion theories),[5,7,8] although Stefan flow induced by evaporation has been included in the analysis. Calculations of this type indicate that interactions can significantly reduce droplet evaporation and burning rates, even for very large droplet spacings.[7,8] For example, for an array of four burning droplets at a spacing of 10 diameters, diffusion theory[7] predicted that the droplet lifetime was increased by 20% over the lifetime of a single isolated droplet. In the presence of forced convection, for the same droplet spacing, the effects of interactions would be negligible, even for a droplet Reynolds number as low as 2.[9,10] In addition to the neglect of forced convection, most investigators also adopted constant-property assumptions. These assumptions resulted in flame sizes that were overpredicted and exceeded experimental values by factors of 3–5.[1] Because larger flames compete more extensively for oxygen, the constant-property models predict much stronger interactions compared to the experimental data.[6] Since most practical sprays involve appreciable droplet Reynolds numbers and large variations of thermodynamic and transport properties in the flowfield, the constant-property diffusion theories appear to have limited utility in the analysis of droplet interactions in combusting fuel sprays except in the interior region of a nondilute spray.

The main objective of the present investigation is to study droplet interactions in forced-convective flows and to provide parametric information on the effects of interactions among droplets. The results should be useful for the modeling of dense-spray phenomena. The present study considers droplet interactions in the presence of forced convection, covering Reynolds numbers of interest for practical sprays, by solving the three-dimensional Navier-Stokes equations for flows through droplet arrays. The arrays considered are monosized and planar, with array planes perpendicular to the approaching flow direction. To better simulate the flow around droplets, variable gas properties are used in the analysis. Numerical results are obtained for a Reynolds number range of 5 to 100, droplet spacings of 2 to 24 diameters, approaching flow oxygen concentrations of 0.1 annd 0.2, and two types of fuel, methanol and *n*-butanol.

Law and colleagues[6] have shown that, for binary droplets subjected to natural convection, observed interaction effects during the initial droplet heating period are considerably greater than theoretical predictions, which do not consider this transient heating. However, in the same study and also Ref. 11, Law and colleagues have also shown that, for a single component fuel at low to moderate pressures, effects of transient heating becomes small after the initial 10–20% of the droplet lifetime. Including transient heating, the analysis will introduce additional complexity, and predictions of droplet interactions will depend on the coupled effects of droplet initial conditions (size, temperature, etc.), approaching flow conditions, the history of vaporization, and the instantaneous droplet size, spacing, and Reynolds number. Quantitative presentation of results and the isolation of individual factors affecting droplet interactions will become more difficult. As a result, only steady-state conditions are considered, and the predictions presented in this paper are applicable to interacting droplets only after the initial heating-up period.

Assumptions

In the most general case, the equations describing the flow include conservation of mass, momentum, energy, and species for both the gas and liquid phases. Additional constitutive relations are the equation of state and the thermodynamic and transport properties as functions of temperature, pressure, and species concentrations. In order to make the problem tractable and to avoid undue complications, the following assumptions are made:

1) The gas-phase processes are quasisteady, i.e., the gas phase adjusts to the steady-state structure for the imposed boundary conditions at each instant of time. This assumption is justified by the large liquid/gas density ratio. Because of the density difference, the liquid-phase properties, e.g., the surface regression rate, surface temperature, and species concentrations, change at rates much slower than those of the gas phase.

2) Liquid-phase internal motion and transient heating are neglected. The droplet remains uniformly at the wet-bulb temperature, which is determined by balancing the heat transfer to the liquid and latent heat of vaporization.

Because of assumptions 1 and 2, the droplet size, spacing, and Reynolds number all remain at their initial values, and transient heating of the droplet is excluded from the analysis. These assumptions offer two very important advantages. First, the detailed flowfield solutions within the liquid droplet become unnecessary, and the only interphase properties sought in the solution procedures are wet-bulb temperature and pressure, from which other interphase boundary conditions (such as fuel vapor concentration) can be calculated. Second and more important, the parametric effect of individual factors affecting droplet interactions can then be studied, without complications caused by simultaneous change of more than one parameter, droplet initial conditions, and the history of vaporization.

3) Phase equilibrium is maintained at the droplet surface. The fuel vapor concentration at the surface is given by the saturated vapor pressure correlation for the pure liquid, e.g., the Clausius-Clapeyron equation, at the wet-bulb temperature. Surface tension corrections are neglected.

4) Effects of thermal radiation and turbulence, as well as Dufour and Soret effects, are neglected. The droplets are spherical. The pressure of the approaching flow is maintained at 1 atm, and the ambient gases have negligible solubility in the liquid phase. The effect of natural convection is also neglected since the Grashof number is generally two orders of magnitude smaller than the square of the Reynolds number for the flows considered in this study.

5) Mass diffusion is represented by an effective binary diffusion law.

6) The chemical reaction rates are much faster than the gas-phase transport rates, so that combustion occurs in a thin flame sheet where fuel and oxygen meet in stoichiometric proportions. The chemical reaction at the flame sheet is assumed to be governed by single-step kinetics of the type

$$\text{fuel} + \text{oxidizer} \rightarrow \text{products}$$

Flames around vaporizing droplets are generally thick, and the flame sheet assumption may not be realistic. This assumption is necessary in this study, however, since the alternative, namely, a finite-rate kinetics model, would be too expensive for the present three-dimensional flow calculations because many additional stiff species equations have to be solved.

7) The mass diffusivities of the combustion products and the fuel vapor are equal. Since the binary diffusivity is only a weak function of species molecular weight, the error introduced by this assumption should be small. Because of assumptions 6 and 7, the gas-phase species concentration field of the burning droplets can be described by one conserved scalar quantity, e.g., the mixture fraction (defined as the fraction of mass that originated from the droplets).

8) Effects of the wake instability are neglected. The onset of wake instability for solid particles in isothermal flow occurs at a Reynolds number around 130, which is greater than the maximum Reynolds number (100) considered in the present study. No information is currently available for the effect of vaporization or combustion on the onset of wake instability.

The foregoing assumptions may become invalid at low pressures (below 1 atm), near the thermodynamic critical point of the fuel, for very small droplets (on the order of 1 μm), or in the presence of luminous flames. It is noted that, in practical sprays, the droplets vaporize and accelerate (decelerate) in the gas-phase flowfield; then, at some time in the life histories of the droplets, their Reynolds numbers will be sufficiently low to make the effect of natural convection important.

Analysis

Governing Equations

The three-dimensional, unsteady Navier-Stokes equations are solved for the asymptotic steady-state flowfield in droplet arrays. The equations are cast in conservation law form and solved using a finite-difference method. To enhance numerical accuracy and efficiency, coordinate mappings are employed that bring droplet surface and symmetric planes onto coordinate surfaces and cluster grid points near the droplet surface. The governing equations, written in the generalized curvilinear coordinates $\xi(x,y,z)$, $\eta(x,y,z)$, and $\zeta(x,y,z)$, are given as follows:[12]

$$\frac{\partial}{\partial t}\hat{q} + \frac{\partial(\hat{E} - \hat{E}_v)}{\partial \xi} + \frac{\partial(\hat{F} - \hat{F}_v)}{\partial \eta} + \frac{\partial(\hat{G} - \hat{G}_v)}{\partial \zeta} = 0 \tag{1}$$

where

$$\hat{q} = J^{-1}\begin{bmatrix} \rho \\ \rho u \\ \rho v \\ \rho w \\ e \\ \rho f \end{bmatrix} \qquad \hat{E} = J^{-1}\begin{bmatrix} \rho U \\ \rho u U + \xi_x p \\ \rho v U + \xi_y p \\ \rho w U + \xi_z p \\ (e + p)U \\ \rho f U \end{bmatrix}$$

$$\hat{F} = J^{-1}\begin{bmatrix} \rho V \\ \rho u V + \eta_x p \\ \rho v V + \eta_y p \\ \rho w V + \eta_z p \\ (e + p)V \\ \rho f V \end{bmatrix} \qquad \hat{G} = J^{-1}\begin{bmatrix} \rho W \\ \rho u W + \zeta_x p \\ \rho v W + \zeta_y p \\ \rho w W + \zeta_z p \\ (e + p)W \\ \rho f W \end{bmatrix} \tag{2}$$

$$\begin{aligned} U &= \xi_x u + \xi_y v + \xi_z w \\ V &= \eta_x u + \eta_y v + \eta_z w \\ W &= \zeta_x u + \zeta_y v + \zeta_z w \end{aligned} \tag{3}$$

where U, V, and W are contravariant velocities, ξ_x, ξ_y, ξ_z, etc., are the metric coefficients, and J is the Jacobian of the coordinate transformation.

The viscous flux terms are given by

$$\hat{E}_v = J^{-1}\begin{bmatrix} 0 \\ \xi_x\tau_{xx} + \xi_y\tau_{xy} + \xi_z\tau_{xz} \\ \xi_x\tau_{yx} + \xi_y\tau_{yy} + \xi_z\tau_{yz} \\ \xi_x\tau_{zx} + \xi_y\tau_{zy} + \xi_z\tau_{zz} \\ \xi_x\alpha_x + \xi_y\alpha_y + \xi_z\alpha_z \\ \xi_x\beta_x + \xi_y\beta_y + \xi_z\beta_z \end{bmatrix} \tag{4}$$

The forms for $\hat{F}_v$ and $\hat{G}_v$ are similar to $\hat{E}_v$, except that ξ is replaced by η and ζ in $\hat{F}_v$ and $\hat{G}_v$, respectively.

The stress and viscous dissipation terms and the species and thermal energy diffusion terms are given by

$$\begin{aligned} \tau_{xx} &= 2\mu u_x - \tfrac{2}{3}\mu(u_x + v_y + w_z) \\ \tau_{xy} &= \tau_{yx} = \mu(u_y + v_x) \\ \tau_{xz} &= \tau_{zx} = \mu(u_z + w_x) \\ \tau_{yy} &= 2\mu v_y - \tfrac{2}{3}\mu(u_x + v_y + w_z) \\ \tau_{yz} &= \tau_{zy} = \mu(v_z + w_y) \\ \tau_{zz} &= 2\mu w_z - \tfrac{2}{3}\mu(u_x + v_y + w_z) \\ \alpha_x &= -q_x + u\tau_{xx} + v\tau_{xy} + w\tau_{xz} \\ \alpha_y &= -q_y + u\tau_{yx} + v\tau_{yy} + w\tau_{yz} \\ \alpha_z &= -q_z + u\tau_{zx} + v\tau_{zx} + w\tau_{zz} \\ \beta_x &= \rho\mathscr{D}_F f_x, \qquad \beta_y = \rho\mathscr{D}_F f_y, \qquad \beta_z = \rho\mathscr{D}_F f_z \\ q_x &= -kT_x - \sum_{i=1}^{N_s} h_i\rho\mathscr{D}_i Y_{ix} \\ q_y &= -kT_y - \sum_{i=1}^{N_s} h_i\rho\mathscr{D}_i Y_{iy} \\ q_z &= -kT_z - \sum_{i=1}^{N_s} h_i\rho\mathscr{D}_i Y_{iz} \end{aligned} \tag{5}$$

where the subscripts x, y, and z denote differentiation in the respective directions. The total internal energy per unit volume and pressure are given by

$$e = \sum_{i=1}^{N_s} \rho h_i Y_i - p + \frac{\rho}{2}(u^2 + v^2 + w^2) \tag{6}$$

$$h_i = h_{fi}^0 + \int_{T_R}^{T} c_{p_i}\, \mathrm{d}T \tag{7}$$

$$P = \rho\tilde{R}T\sum_{i=1}^{N_s}\frac{Y_i}{M_i} \tag{8}$$

where h_{fi}^0 is the heat of formation for species i at the reference temperature T_R. The Cartesian derivatives are to be evaluated in ξ,η,ζ space via the chain rule, for example,

$$T_x = \xi_x T_\xi + \eta_x T_\eta + \zeta_x T_\zeta$$

Thermodynamic and Transport Properties

Thermodynamic and transport properties at each grid point in the flowfield are calculated using temperatures and species concentrations calculated at the previous time step. The specific heat, thermal conductivity, and viscosity for each species are determined by polynomials of temperature, such as

$$C_{p_i} = A_i + B_i T + C_i T^2 + D_i T^3 \tag{9}$$

The coefficients of these polynomials are found in Ref. 13. The specific heat of the gas mixture is obtained by concentration weighting of each species. The thermal conductivity and viscosity of the mixture, however, are calculated using Wilke's law;[14] for example, the mixture viscosity is determined by

$$\mu = \sum_{i=1}^{N_s} \frac{\mu_i}{1 + 1/X_i \sum\limits_{\substack{j=1 \\ j \neq i}}^{N_s} X_j\varphi_{ij}} \tag{10}$$

where

$$\varphi_{ij} = \frac{[1 + (\mu_i/\mu_j)^{\frac{1}{2}}(M_j/M_i)^{\frac{1}{4}}]^2}{2\sqrt{2}[1 + M_i/M_j]^{\frac{1}{2}}} \tag{11}$$

The binary mass diffusivity for the fuel vapor in the ambient gas is obtained using the Chapman-Enskog theory in conjunction with the Lennard-Jones intermolecular potential-energy functions. Details of this method can be found in Ref. 14.

Combustion Model

Both droplet evaporation and combustion are considered in the present study. For the burning droplet case, a mixing-controlled combustion model is employed. Chemical reaction rates are assumed to be much faster than gas-phase mixing rates, and the chemical reactions proceed immediately to completion when the fuel vapor and the oxidizer are mixed in stoichiometric proportions. The flame front positions are determined from the stoichiometric mixture fraction values. The concentrations of the unburned fuel vapor, combustion products, oxygen, and nitrogen (assuming the approaching flow is composed of only oxygen and nitrogen) can then be determined by the mixture fraction and the flame front location. Denoting the stoichiometric coefficient (by mass) of oxygen as v and the oxygen mass concentration in the approaching flow as Ω, the stoichiometric mixture fraction value and the species concentrations in the gas mixture can be calculated from

$$f_{\text{stoic}} = \frac{1}{1 + v/\Omega} \tag{12}$$

from the droplet surface to the flame front,

$$\begin{aligned} [Y_{\text{prod}}] &= \Omega(1-f)(1+1/v) \\ [Y_{N2}] &= (1-\Omega)(1-f) \\ [Y_{02}] &= 0 \\ [Y_{\text{UF}}] &= 1 - [Y_{\text{prod}}] - [Y_{N2}] - [Y_{02}] \end{aligned} \tag{13}$$

and from the flame front to the outer edge of the flow domain,

$$\begin{aligned} [Y_{\text{prod}}] &= f(1+v) \\ [Y_{N2}] &= (1-\Omega)(1-f) \\ [Y_{\text{UF}}] &= 0 \\ [Y_{02}] &= 1 - [Y_{\text{prod}}] - [Y_{N2}] - [Y_{\text{UF}}] \end{aligned} \tag{14}$$

After the concentration field is obtained, temperatures and pressures are calculated from Eqs. (6–8), using Newton's iteration method.

Surface Integral Parameters

Previous numerical and experimental studies on drag and heat and mass transport for isolated droplets in high-temperature flows are abundant.[15] Results from these studies are used to validate the current analysis described in this paper. Since results were presented in the form of drag coefficients and Nusselt numbers for most of the existing studies, these integral parameters are also calculated in the present study to facilitate comparison.

The drag force on the liquid droplet consists of contributions from the viscous stresses, the pressure, and the momentum flux due to vaporization at the interface. The computed momentum flux force (the thrust drag) at the droplet surface is about two orders of magnitude smaller than the other two forces and is therefore neglected. If grid orthogonality is maintained at the surface, the axial (approaching flow direction) component of the surface shear stresses can be written, in terms of variables in the curvilinear coordinates (ξ,η,ζ), as

$$\begin{aligned} F_f = {} & \mu\left(\frac{\partial\hat{U}/\partial\zeta}{\sqrt{g_{\zeta\zeta}}} + \frac{\partial\hat{W}/\partial\xi}{\sqrt{g_{\xi\xi}}} + \frac{\partial\hat{U}/\partial\eta}{\sqrt{g_{\eta\eta}}} + \frac{\partial\hat{V}/\partial\xi}{\sqrt{g_{\xi\xi}}}\right)\frac{x_\xi}{\sqrt{g_{\xi\xi}}} \\ & + \mu\left(\frac{\partial\hat{W}/\partial\zeta}{\sqrt{g_{\zeta\zeta}}} - \tfrac{2}{3}\Delta\right)\frac{x_\zeta}{\sqrt{g_{\zeta\zeta}}} \end{aligned} \tag{15}$$

where

$$\hat{U} = \frac{U}{\sqrt{\xi_x^2 + \xi_y^2 + \xi_z^2}}$$

$$\hat{V} = \frac{V}{\sqrt{\eta_x^2 + \eta_y^2 + \eta_z^2}}$$

$$\hat{W} = \frac{W}{\sqrt{\zeta_x^2 + \zeta_y^2 + \zeta_z^2}}$$

$$g_{\xi\xi} = x_\xi^2 + y_\xi^2 + z_\xi^2$$

$$\begin{aligned} \Delta = {} & (\xi_x u_\xi + \xi_y v_\xi + \xi_z w_\xi) + (\eta_x u_\eta + \eta_y v_\eta + \eta_z w_\eta) \\ & + (\zeta_x u_\zeta + \zeta_y v_\zeta + \zeta_z w_\zeta) \end{aligned}$$

is the rate of dilation. The expressions for $g_{\eta\eta}$ and $g_{\zeta\zeta}$ are similar to $g_{\xi\xi}$.

The axial component of the pressure force is

$$F_p = -p\frac{X_\zeta}{\sqrt{g_{\zeta\zeta}}} \tag{16}$$

Integrating over the droplet surface and nondimensionalizing with approaching flow quantities, the drag coefficient becomes

$$C_D = \frac{1}{\pi \mathrm{d}_p^2(\rho u_\infty^2/8)} \int_{\xi=1}^{\xi_{\max}} \int_{\eta=1}^{\eta_{\max}} (F_f + F_p)\sqrt{g_{\xi\xi}g_{\eta\eta} - g_{\xi\eta}^2}\,\mathrm{d}\xi\,\mathrm{d}\eta \tag{17}$$

where $g_{\xi\eta} = x_\xi x_\eta + y_\xi y_\eta + z_\xi z_\eta$.

To be consistent with most of the published data, the Nusselt and Prandtl numbers are calculated using the film properties, i.e.,

$$Nu = \frac{Hd_p}{k_m}, \qquad Pr = \frac{C_{Pm}\mu_m}{k_m}$$

where the subscript m refers to the film condition defined by $\alpha = 1/2$ in the following equations:

For vaporizing droplets:

$$\begin{aligned} T_m &= \alpha T_s + (1-\alpha)T_\infty \\ Y_m &= \alpha Y_s + (1-\alpha)Y_\infty \end{aligned} \tag{18}$$

For burning droplets:

$$\begin{aligned} T_m &= \alpha T_s + (1-\alpha)T_{\text{flame}} \\ Y_m &= \alpha Y_s + (1-\alpha)Y_{\text{flame}} \end{aligned}$$

The heat-transfer coefficient is given

For evaporating droplets:

$$H = \frac{k(\partial T/\partial r_s)}{(T_\infty - T_s)}$$

For burning droplets:

$$H = \frac{k(\partial T/\partial r_s)}{(T_{\text{flame}} - T_s)} \tag{19}$$

where the derivative $\partial/\partial r$, for orthogonal grids at the surface, is given by

$$\frac{\partial}{\partial r} = \frac{\partial/\partial\zeta}{\sqrt{g_{\zeta\zeta}}}$$

Numerical Methods

Grid System

Two-dimensional planar arrays of equally spaced droplets are employed in the present study. A schematic of a typical array configuration is shown in Fig. 1. Because of the symmetric arrangement of droplets, only a 45-deg sector, as indicated in Fig. 1, needs to be considered in the computation. To enhance numerical accuracy and efficiency, coordinate mappings are used that bring droplet surface and symmetry planes onto

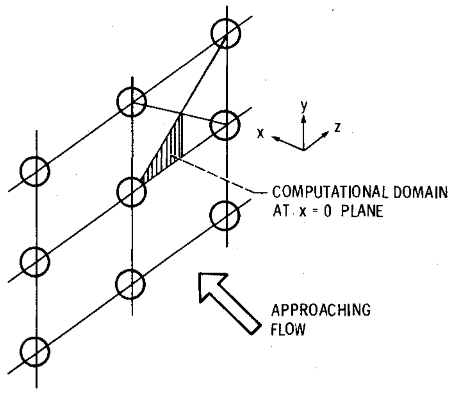

Fig. 1 Schematic of the two-dimensional droplet array.

Fig. 2 Grid system.

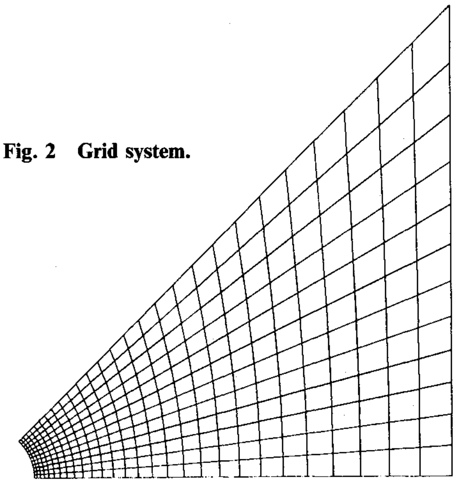

(a) Vertical plane (x = 0), perpendicular to approaching flow.

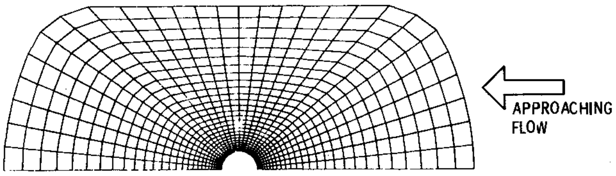

(b) Meridional plane (y = 0).

coordinate surfaces and cluster grid points near the droplet surface. This would also help the implementation of boundary conditions since no interpolations are required at boundary surfaces. An O-type grid, as shown in Fig. 2, is generated algebraically, with a minimum radial spacing (in the physical domain) of 0.02 droplet radius, and the grids are stretched exponentially in the radial direction outward from the droplet surface. For clarity of presentation, much larger grid spacings near the droplet surface and fewer grid lines are shown in Fig. 2 than were actually used in the calculations. Grid orthogonality is maintained at and near the droplet surface so that the interphase heat and mass fluxes and the shear stresses can be easily calculated. In the curvilinear coordinates, the computational domain is rectangular parallelpiped with uniform grid spacing, which facilitates the use of standard unweighted differencing schemes and helps to maintain higher-order numerical accuracy. Most of the calculations in the present study are performed using a 55 × 15 × 55 grid in the axial (approaching flow), azimuthal, and radial directions, respectively. Fifteen grid lines in the azimuthal direction are considered adequate for spatial resolution since the flow domain (only 45 deg) and the gradients of flow properties are smaller in this direction than in the other two directions. The grid is reduced to 41 × 12 × 41 for the lowest Reynolds number case ($Re = 5$) owing to the numerical instability in the finer grid. One calculation for $Re = 100$ using a 65 × 18 × 65 grid was performed and showed negligible improvement over the results obtained using the 55 × 15 × 55 grid. Therefore, it may be concluded that the numerical solutions are relatively independent of the grid density.

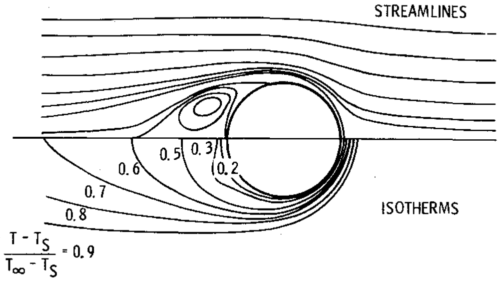

Fig. 3 Streamlines and isotherms of an isolated vaporizing methanol droplet for $T_\infty = 800$ K and Re = 100 at meridional plane ($y = 0$).

Finite-Difference Procedure

The finite-difference scheme used for solving the governing equations is the delta-form implicit approximate factorization algorithm described by Beam and Warming.[16] Since this and other similar schemes are fully documented in the literature,[12,16,17] only a very brief discussion of the numerical method will be given here. Because only the asymptotic steady-state solutions are required, a first-order Euler implicit scheme is used to integrate the unsteady Navier-Stokes equations in time. The spatial derivative terms are approximated with fourth-order central differences. Fourth-order explicit and second-order implicit artificial dissipation terms are added to the basic central-differencing algorithm to control the nonlinear numerical instability.[18] Local time linearizations are applied to the nonlinear terms,[16] and an approximate factorization of the three-dimensional implicit operator is used to produce locally one-dimensional finite-difference operators.[16,17] The resulting operators are block pentadiagonal matrices, and their inversion, although much easier than the unfactorized operators, accounts for the major portion of the total computational effort of the implicit scheme. To improve the numerical efficiency, a similarity transformation[19] is employed that diagonalizes the blocks in the implicit scheme and produces scalar pentadiagonal operators in place of the block operators.

Boundary Conditions

The boundary conditions are implemented explicitly. The velocity, temperature, static pressure, and species concentrations are specified for the approaching flow. At the downstream plane where the flow leaves the computational domain, flow properties are extrapolated from interior points except for the static pressure, which is set equal to the approaching flow value. These upstream and downstream boundary conditions are applied at a distance of 25 diameters from the center of the droplet. At the midplanes between the droplets, symmetry conditions are applied. The droplet surface mass flux due to gasification is given by

$$\rho U_s = -\rho \mathscr{D}_F \frac{(\partial Y_F / \partial r)_s}{(1 - Y_{Fs})} \tag{20}$$

and the gas velocity components at the surface are obtained accordingly. The pressure on the droplet surface is calculated with a normal momentum relation (obtained by combining the three momentum equations).[12] The droplet surface temperature is taken as the wet-bulb temperature, which is obtained from the balance of the total heat transfer to the surface and

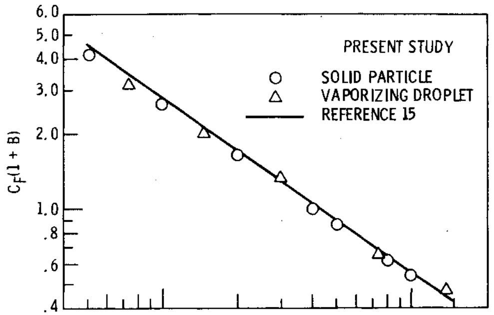

(a) Friction drag coefficient.

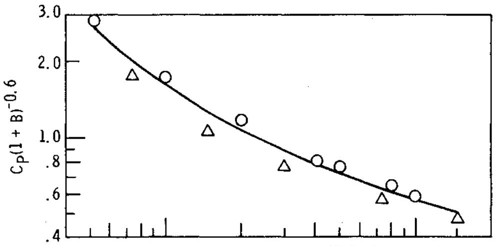

(b) Pressure drag coefficient.

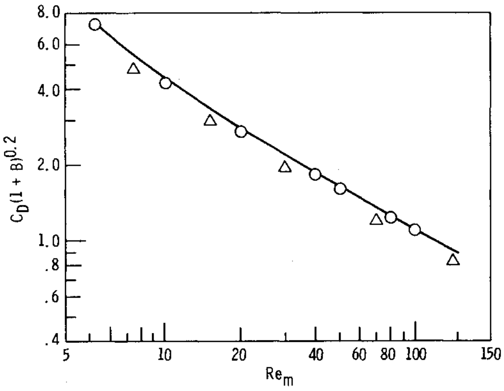

(c) Total drag coefficient.

Fig. 4 Drag coefficients for isolated solid particles and evaporating droplets.

the latent heat of vaporization and, therefore, is part of the solution. The surface fuel vapor concentration Y_{Fs} is obtained from the partial pressure of the saturated fuel vapor at the wet-bulb temperature using the Clausius-Clapeyron equation. For the case of droplet evaporation (nonburning), the gas phase is considered as a binary mixture of fuel vapor and air, and the mixture fraction f is equivalent to the fuel vapor concentration; hence, $f_s = Y_{Fs}$ and $Y_{As} = 1 - Y_{Fs}$ at the droplet surface. For burning droplets, the surface mixture fraction is calculated by

$$f_s = Y_{Fs} + f_{\text{stoic}}(1 - Y_{Fs}) \tag{21}$$

where f_{stoic} is given by Eq. (12). Concentrations of the remaining species at the surface are obtained using Eq. (13).

Results and Discussion

Calculations are first made for single, isolated solid particles and evaporating droplets, where the abundance of existing experimental and numerical data facilitates the validation of the analysis described in previous sections. The streamlines and isotherms for an isolated methanol droplet in a hot airstream at a temperature of 800 K, a particle Reynolds number of 100, and a pressure of 1 atm are shown in Fig. 3. There is a recirculation region (wake) formed behind the droplet, and the reattachment point at the axis ($\theta = \pi$) is located at 0.96 diameter from the rear stagnation point. The isotherms show steep gradients near the front stagnation point, indicating that the heat-transfer rate is higher at the front half of the sphere. The locations of the reattachment points behind solid particles in isothermal flows were also calculated for Reynolds numbers 20–100. The predictions (not shown here) agree very well with the calculations of Rimon and Cheng[20] and the experimental data quoted therein. As an example, the present calculations show that the reattachment distance for a solid particle at an Re of 100 was 0.92 diameter, compared to the value of about 0.90 diameter reported in Ref. 20.

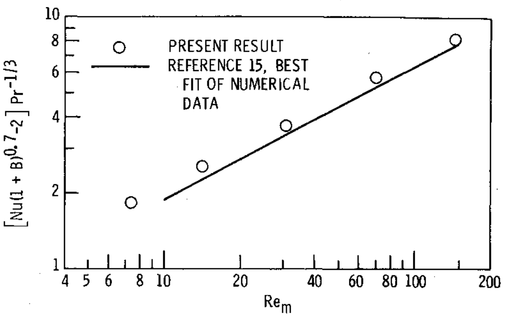

Fig. 5 Numerical heat-transfer data for isolated droplets.

The drag of isolated solid particles in isothermal flows and the drag and heat transfer of isolated evaporating droplets in hot streams at a temperature of 1000 K are compared with numerical results reported by Renksizbulut and Yuen.[15] The friction, pressure, and total drag coefficients are shown in Fig. 4, and the heat-transfer results in Fig. 5. The Reynolds number and B number appearing in these two figures are defined as $\rho_\infty q_\infty d_p/\mu_m$ and $C_{Pm}(T_\infty - T_s)/h_{fg}$, respectively. The agreement between the present calculations and the results in Ref. 15 is very good. Since the numerical results in Ref. 15 correlate well with a wide range of experimental data, the present numerical results also are in good agreement with experimental data. Figures 4 and 5 also indicate that the standard drag law and the conventional empirical expressions for Nusselt number can be used for evaporating droplets in flows with large variations of transport properties, provided the proper film properties are chosen for evaluation of Reynolds number and the heat-transfer number B.

Law and colleagues[1,6] have indicated that flame size and ambient oxygen concentration are the major factors in determining the extent of interactions for burning droplets. The flame shapes for single, isolated methanol and n-butanol droplets at $Re = 25$ are illustrated in Figs. 6a and 6b, respectively. Approaching flow oxygen concentrations of 0.1 and 0.2 are considered. Since the stoichiometric mixture fraction of n-butanol is smaller than that of methanol, the flame size of the former is larger than the latter, especially near the wake, where the high mixture fraction region extends to several diameters downstream of the rear stagnation point. The influence of oxygen concentration on flame size is also illustrated in Figs. 6a and 6b. For the lower oxygen concentration ambient flow, the stoichiometric condition occurs at a greater distance from the droplet surface. This, in turn, will yield a larger flame standoff distance for the lower oxygen concentration case. The same figures also show that, along the direction of the front stagnation line, the flame is situated at a larger distance for the higher oxygen case. This is caused by the intense blowing of fuel vapor against the approaching flow owing to the proximity of the flame. For the higher oxygen case, the flame temperature is higher and the resulting blowing is stronger; this, in turn, pushes fuel vapor farther upstream and yields a larger flame distance along the front stagnation line.

Another important aspect in droplet transport analysis is the evaluation of physical properties for the gas mixture around the droplets.[1,6,15] To illustrate the importance of physical properties, the gas-phase thermal conductivity, the viscosity, and the product of density and fuel vapor mass diffusivity in the $\theta = 90$ deg plane, normalized by the surface properties, are

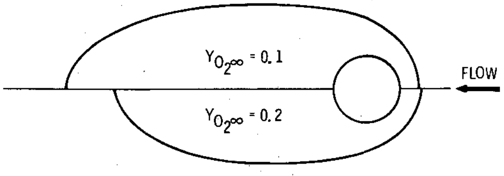

(a) Methanol droplet.

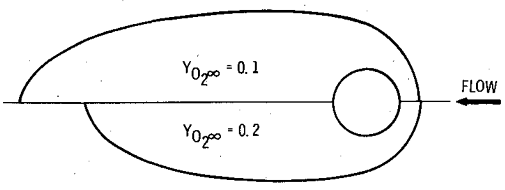

(b) n-Butanol droplet.

Fig. 6 Flame shape for isolated droplet at *Re* = 25.

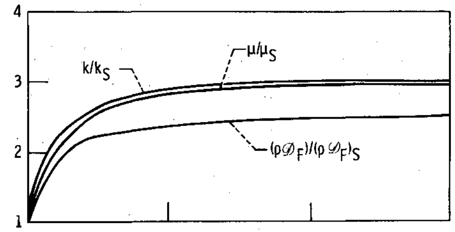

(a) Evaporating droplet, $T_\infty = 1000$ K.

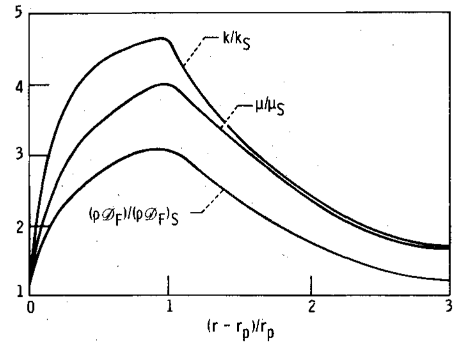

(b) Burning droplet, $Y_{O_2\infty} = 0.2$ $T_\infty = 400$ K.

Fig. 7 Normalized gas mixture transport properties for isolated methanol droplet at $\theta = 90$ deg plane, *Re* = 50.

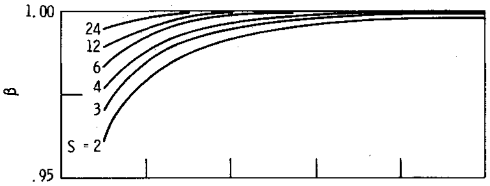

(a) $T_\infty = 700$ K.

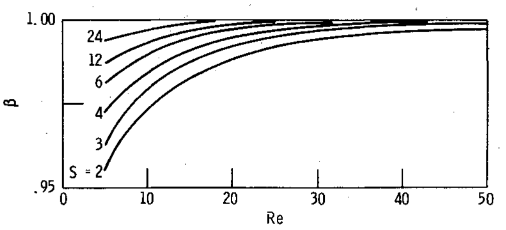

(b) $T_\infty = 1400$ K.

Fig. 8 Gasification rate correction factor for evaporating methanol droplets.

plotted against radial distance in Figs. 7a and 7b for an isolated droplet undergoing evaporation (Fig. 7a) or burning (Fig. 7b). The figures clearly show that, in numerical simulations, if physical properties are taken to be constant and evaluated at the freestream (evaporation case) or flame (burning case) conditions, droplet transport rates will be significantly overestimated compared to the variable-property approach. Law and colleagues[1,6] have also pointed out that, for isolated droplets, because of constant-property assumptions, theoretical predictions of the flame size consistently exceed experimental values by factors of 3–5.

The results shown in Figs. 3–5 have demonstrated the validity of the present analysis and numerical procedures. Calculations of the interacting droplets are considered next. The droplet assemblages considered are planar arrays of equally spaced monosized droplets. The arrays are oriented perpendicular to the approaching flow direction. In the following, the effects of interactions are presented as a gasification rate correction factor:

$$\beta = \frac{\text{rate of gasification of a droplet in an array}}{\text{rate of gasification of an isolated droplet}}$$

The gasification rate correction factors for evaporating (nonburning) methanol droplets are shown in Figs. 8a and 8b for $T_\infty = 700$ and 1400 K, respectively. As seen in Fig. 8, droplet interactions are only important for small spacings and low Reynolds numbers. They become negligible for spacings greater than about 6 diameters and Reynolds numbers greater than about 10. The present calculations show much weaker and shorter-ranged interactions than predicted by the diffusion theories,[7,8] where the effect of forced convection is not considered. A close inspection of the predicted flowfield indicates that, in the presence of forced convection, temperature and concentration variations are contained in a boundary layer around the droplet and that the approaching stream conditions prevail outside this boundary layer. Since the boundary-layer thickness around the droplet is of the order of magnitude of one droplet-diameter for the Reynolds numbers considered here, the effects of neighboring droplets on evaporation are not likely to be very significant for droplet spacings much greater than one diameter.

Figures 8a and 8b indicate that the results are very similar for ambient temperatures of 700 and 1400 K. The higher ambient temperature, shown in Fig. 8b, yields a slightly stronger interaction between droplets. The thicker thermal and concentration boundary layers and the stronger competition among neighboring droplets for thermal energy caused by the more intense evaporation at the higher temperature are responsible for the increased interactions between droplets at the higher temperature.

The gasification rate correction factors for burning methanol droplets are shown in Figs. 9a and 9b, for approaching flow oxygen concentrations of 0.1 and 0.2, respectively. The interactions are stronger than the results previously shown in Figs. 8a and 8b for the evaporating droplets. This is attributed to the higher gasification rate due to the presence of the flame and the competition for oxygen by neighboring flames. The lower ambient oxygen concentration case also shows stronger interactions than the higher ambient oxygen concentration case as shown in Figs. 9a and 9b. As previously discussed in Fig. 6, the flame size is larger in the lower ambient oxygen concentration stream, which increases competition for oxygen by neighboring flames and results in stronger interactions.[6] It can be clearly seen in both Figs. 9a and 9b that, in contrast to the findings based on the diffusion theories,[7,8] the effects of interactions between droplets diminish rapidly for droplet spacings greater than about 6 diameters and Reynolds numbers greater than about 10. The stronger and longer-ranged interactions obtained by the diffusion theory are caused chiefly by the neglect of forced convection and the use of constant properties in the analysis.

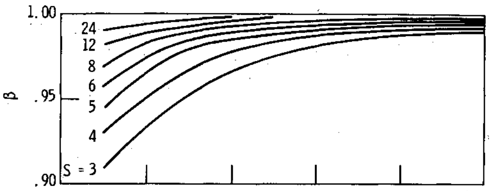

(a) $Y_{O_2\infty} = 0.1.$

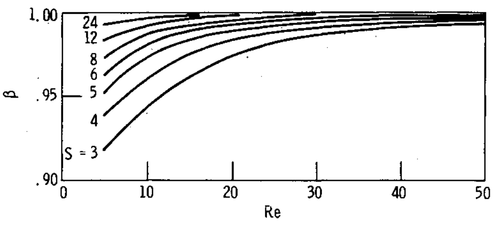

(b) $Y_{O_2\infty} = 0.2.$

Fig. 9 Gasification rate correction factor for burning methanol droplets.

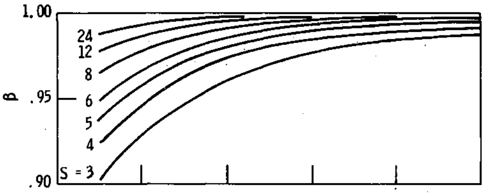

(a) $Y_{O_2\infty} = 0.1.$

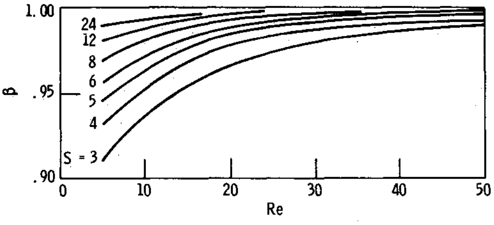

(b) $Y_{O_2\infty} = 0.2.$

Fig. 10 Gasification rate correction factor for burning *n*-buthanol droplets.

The burning rate correction factors for *n*-butanol droplets are shown in Figs. 10a and 10b. The differences between Figs. 10a and 10b are similar to those previously illustrated in Figs. 9a and 9b, i.e., larger flame size in the lower ambient oxygen case yields stronger interactions between droplets. Figures 10a and 10b show that *n*-butanol droplets experience slightly stronger interaction effects than methanol droplets under the same flow conditions. This can again be explained on the basis of flame size in that the larger flames of the *n*-butanol droplets (as shown in Figs. 6a and 6b) compete more vigorously for oxygen since they are physically closer than the smaller flames of the methanol droplets.

The effects of droplet interactions on droplet drag are also investigated in the present study. The blockage of flow by the adjacent droplets accelerates the flow (venturi effect) and produces larger shear stresses as well as a larger wake. This results in a slight increase in friction and pressure drag. The increase in drag due to the venturi effect, however, is mitigated somewhat by the reduction in the boundary-layer viscosity resulting from lower temperatures of the fluid around the interacting droplets (owing to the competition for thermal energy for evaporating droplets and larger flame standoff distances for burning droplets). The net result is an insignificant change in drag due to interactions between droplets.

Conclusions

In the present study, we have investigated the effects of interactions between droplets on the drag and gasification rates of evaporating and burning droplet arrays. The arrays considered are planar, oriented perpendicular to the approaching flow, and composed of equally spaced monosized droplets of the same fuel type. The following conclusions can be drawn.

1) The present analysis predicts less intense and much shorter-ranged droplet interaction effects than those previously obtained using the diffusion theories. The present analysis considers forced-convection and variable-property effects, whereas both are generally neglected in the diffusion theories. Since most practical sprays have appreciable droplet Reynolds numbers and involve large property variations, the present analysis appears to have more relevance for consideration of droplet interactions.

2) The effects of droplet interactions are stronger for fuels and ambient oxygen concentrations that produce larger flame sizes and thereby increase competition for oxygen between droplets. Low ambient oxygen concentration and fuels with smaller stoichiometric fuel mass fractions tend to increase the level of droplet interaction.

3) The effects of droplet interactions on drag are small for the array configuration considered in the present study.

Arrays with droplets aligned along the flow direction are not considered in the present study. For droplet Reynolds numbers encountered in practical sprays, the wake can extend to more than one droplet diameter downstream of the rear stagnation point, and the wake flame is even longer. Droplet interaction effects for such arrays are likely to be significant and warrant further study.

References

[1] Law, C. K., "Recent Advances in Droplet Vaporization and Combustion," *Progress in Energy and Combustion Science*, Vol. 8, No. 3, 1982, pp. 171–201.

[2] Faeth, G. M., "Evaporation and Combustion of Sprays," *Progress in Energy and Combustion Science*, Vol. 9, 1983, pp. 1–76.

[3] Sirignano, W. A., "Fuel Droplet Vaporization and Spray Combustion Theory," *Progress in Energy and Combustion Science*, Vol. 9, 1983, pp. 291–322.

[4] Sangiovanni, J. J. and Kesten, A. S., "Effect of Droplet Interaction on Ignition in Mono-dispersed Droplet Streams," *Proceedings of the 16th International Symposium on Combustion*," Combustion Inst., Pittsburgh, PA, 1977, pp. 577–590.

[5] Chiu, H. H. and Liu, T. M., "Group Combustion of Liquid Droplets," *Combustion Science and Technology*, Vol. 17, 1977, pp. 127–142.

[6] Xiong, T. Y., Law, C. K., and Miyasaka, K., "Interactive Vaporization and Combustion of Binary Droplet Systems," *Proceedings of the 20th International Symposium on Combustion*," Combustion Inst., Pittsburgh, PA, 1985, pp. 1781–1787.

[7] Labowsky, M., "Calcuation of the Burning Rates of Interacting Fuel Droplets," *Combustion Science and Technology*, Vol. 22, No. 5–6, 1980, pp. 217–226.

[8] Marberry, M., Ray, A. K., and Leung, K., "Effect of Multiple Particle Interactions on Burning Droplets," *Combustion and Flame*, Vol. 57, Sept. 1984, pp. 237–245.

[9] Soo, S. -L., *Fluid Dynamics of Multiphase Systems*, Blaisdell, Waltham, MA, 1967, pp. 185–190.

[10] Happel, J. and Brenner, H., *Low Reynolds Number Hydrodynamics*, 2nd rev. ed., Noordhoff, Leiden, the Netherlands, 1973, pp. 240–269.

[11] Law, C. K. and Sirignano, W. A., "Unsteady Droplet Combustion with Droplet Heating—II: Conduction Limit," *Combustion and Flame*, Vol. 28, 1977, pp. 175–186.

[12] Pulliam, T. H. and Steger, J. L., "Implicit Finite-Difference Simulations of Three-Dimensional Compressible Flow," *AIAA Journal*, Vol. 18, Feb. 1980, pp. 159–167.

[13] Yaws, C. L., *Physical Properties*, McGraw-Hill, New York, 1977, pp. 198–215.

[14] Reid, R. C., Prausnitz, J. M., and Sherwood, T. K., *The Properties of Gases and Liquids*, 3rd ed., McGraw-Hill, New York, 1977, pp. 548–550.

[15] Renksizbulut, M. and Yuen, M. C., "Numerical Study of Droplet Evaporation in a High-Temperature Stream," *Journal of Heat Transfer*, Vol. 105, May 1983, pp. 389–397.

[16] Beam, R. M. and Warming, R. F., "An Implicit Finite-Difference Algorithm for Hyperbolic Systems in Conservation-Law Form," *Journal of Computational Physics*, Vol. 22, Sept. 1976, pp. 87–110.

[17] Pulliam, T. H. and Steger, J. L., "Recent Improvements in Efficiency, Accuracy, and Convergence for Implicit Approximate Factorization Algorithms," AIAA Paper 85-0360, Jan. 1985.

[18] Pulliam, T. H. "Artificial Dissipation Models for the Euler Equations," AIAA Paper 85-0438, Jan. 1985.

[19] Pulliam, T. H. and Chaussee, D. S., "A Diagonal Form of an Implicit Approximate-Factorization Algorithm," *Journal of Computational Physics*, Vol. 39, Feb. 1981, pp. 347–363.

[20] Rimon, Y. and Cheng, S. I., "Numerical Solution of a Uniform Flow over a Sphere at Intermediate Reynolds Numbers," *Physics of Fluids*, Vol. 12, May 1969, pp. 949–959.